Magnetic-resonance pore imaging of nonsymmetric microscopic pore shapes

Stefan Andreas Hertel,[1] Xindi Wang,[2] Peter Hosking,[2] M. Cather Simpson,[3] Mark Hunter,[1,4] and Petrik Galvosas[1,*]

[1]*MacDiarmid Institute for Advanced Materials and Nanotechnology, School of Chemical and Physical Sciences, Victoria University of Wellington, Wellington 6140, New Zealand*

[2]*The Photon Factory and the School of Chemical Sciences, The University of Auckland, Auckland 1010, New Zealand*

[3]*The Photon Factory, Department of Physics and School of Chemical Sciences, The University of Auckland, Auckland 1010, New Zealand*

[4]*Magritek Limited, 32 Salamanca Road, Wellington 6012, New Zealand*

(Received 27 December 2014; published 13 July 2015)

Imaging of the microstructure of porous media such as biological tissue or porous solids is of high interest in health science and technology, engineering and material science. Magnetic resonance pore imaging (MRPI) is a recent technique based on nuclear magnetic resonance (NMR) which allows us to acquire images of the average pore shape in a given sample. Here we provide details on the experimental design, challenges, and requirements of MRPI, including its calibration procedures. Utilizing a laser-machined phantom sample, we present images of microscopic pores with a hemiequilateral triangular shape even in the presence of NMR relaxation effects at the pore walls. We therefore show that MRPI is applicable to porous samples without *a priori* knowledge about their pore shape and symmetry. Furthermore, we introduce "MRPI mapping," which combines MRPI with conventional magnetic resonance imaging (MRI). This enables one to resolve microscopic pore sizes and shapes spatially, thus expanding the application of MRPI to samples with heterogeneous distributions of pores.

DOI: 10.1103/PhysRevE.92.012808 PACS number(s): 89.90.+n, 87.61.−c, 61.43.Gt, 82.56.Lz

I. INTRODUCTION

Nuclear magnetic resonance (NMR) methods, including magnetic resonance imaging (MRI), are routinely used to study the structure of porous materials such as biological tissue or porous rocks, providing a unique contrast noninvasively [1]. However, because of its fundamental resolution limitations [2], the use of MRI may be restricted for pore structures on the micrometer scale or below. Intrestingly, these limitations do not affect diffusive-diffractive pulsed gradient spin-echo (PGSE) NMR, which is more akin to scattering than to imaging methods [3]. As such, this method is able to acquire the diffractogram of the pore system via NMR visible fluids located in and saturating the voids of the sample. Since the molecules constituting these pore fluids undergo Brownian motion, they probe the pore space and return structural information of the material under study [3]. Unfortunately, diffusive-diffractive PGSE NMR fails to measure the phase of the detected signal, thus preventing one from obtaining pore images via straightforward Fourier inversion of the measured diffractograms. Other scattering techniques such as x-ray [4] and neutron scattering [5] share this shortcoming which is commonly referred to as the "phase problem." However, recent advances in PGSE NMR techniques have overcome this fundamental issue. In 2011 Laun *et al.* suggested a modification of a single PGSE NMR experiment to acquire images of arbitrary pore shapes [6]. More recently Ref. [7] introduced a synergistic approach using two double PGSE NMR experiments. It enables one to obtain the full form factor, although it remains limited to certain pore symmetries [8]. This method was later extended to arbitrary pore geometries by restoring the phase and amplitude information of the signal via iterative approaches at reduced signal-to-noise ratios [9]. Hertel *et al.* suggested the name magnetic resonance pore imaging (MRPI) for the approach of Laun *et al.* and demonstrated its feasibility on cylindrical microcapillaries by obtaining images of the average pore with a nominal spatial resolution of only 1.3 μm [10]. Independently, Kuder *et al.* showed that the MRPI approach is working for millimeter-sized triangular capillaries utilizing hyperpolarized xenon gas and therefore showed the applicability of the method for arbitrary pore geometries [11]. However, the proof of feasibility of MRPI on the micrometer scale for nonpoint symmetric pore shapes remained an open challenge to date.

In this work we meet this challenge using a laser-machined microcapillary array with hemiequilateral triangular pore shapes. We will provide a detailed description of the MRPI pulse sequence, including a thorough discussion of the experimental implementation of MRPI in extension of our previous communication [10]. The application of the pulse sequence to two-dimensional (2D) MRPI will be discussed and the observed effects of blurring and edge enhancement will be analyzed in detail. Using the hemiequilateral triangular capillary sample we show for the first time that one can obtain the full complex form factor (returning the pore shape via its Fourier transform) of nonpointsymmetric pores on the micrometer scale. Furthermore, we introduce a novel approach we name "MRPI mapping," which combines MRPI with MRI by measuring and analyzing the MRPI signal with respect to individual voxels of the MRI image.

II. THEORY AND DESCRIPTION OF MRPI

A. Principle

When studying porous materials it is convenient to describe pore shapes by its Fourier transform leading to a complex function called the form factor,

$$S_0(\boldsymbol{q}) = \int_V \rho_0(\boldsymbol{r}) e^{-i2\pi \boldsymbol{q}\cdot\boldsymbol{r}}\, d\boldsymbol{r}, \tag{1}$$

*petrik.galvosas@vuw.ac.nz

where $\rho_0(\boldsymbol{r})$ is the pore shape function, $\boldsymbol{q}$ is the wave vector in units of m^{-1} and V is the volume of the pore space [4,12]. In NMR experiments the pore shape $\rho_0(\boldsymbol{r})$ is equal to the spin-density function under the assumption of a homogeneously filled pore with a fluid containing NMR active nuclei. To describe an array of pores, rather than a single pore one may require the so-called structure factor as well. This function captures the scattering intensity due to the arrangement of pores on a lattice [5]. Indeed, first reports on diffusive-diffraction PGSE NMR measured the averaged squared structure factor of a connected pore system resembling a lattice of pores [3,13]. In these studies the observed diffraction peak in the PGSE NMR spin-echo decay can be explained in terms of the lattice constant due to the distance of neighboring pores. However, in later studies it has been shown that this method can also be utilized to measure the average squared form factor of closed pore systems [14–16]. Unfortunately. this may have led to confusion of terms in recent publications where the form factor $S_0(\boldsymbol{q})$ is called the structure factor [10] or structure function [7].

PGSE NMR techniques allow access to features of the form factor by measuring the NMR signal at different wave vectors $\boldsymbol{q} = \gamma\delta\boldsymbol{G}/2\pi$ imposed onto the spin system [3]. Here γ is the gyromagnetic ratio of the observed nucleus, δ is the length of the gradient pulses, and $\boldsymbol{G}$ is the gradient vector. In such experiments the normalized spin-echo amplitude $E = M(q)/M(q=0)$ is given by the ensemble average of the phase Φ that the spins acquire during the NMR diffusion experiment [17,18],

$$E = \langle \exp\{-i\Phi\} \rangle. \tag{2}$$

The ensemble average $\langle \dots \rangle$ has to be taken over all spins contributing to the signal formation and can be replaced by the volume integral over the spin-density function $\langle \dots \rangle = 1/V \int_V \dots \rho_0(\boldsymbol{r})\, d\boldsymbol{r}$. Since for each closed pore a similar expression can be found, we restrict ourselves to one representative pore.

The common principle of PGSE-based methods (including MRPI) is the superposition of the polarizing magnetic field B_0 in the z direction with a pulsed field gradient $\boldsymbol{G}(t)$ [19,20], such that the magnetic field at time t and position $\boldsymbol{r}(t)$ is given by $B_z(\boldsymbol{r},t) = B_0 + \boldsymbol{G}(t)\cdot\boldsymbol{r}(t)$. Throughout this study we regard only the z direction of the magnetic field and define the magnetic field gradient as $\boldsymbol{G} = (\partial B_z/\partial x, \partial B_z/\partial y, \partial B_z/\partial z)$. Thus, we chose to leave out the index z in the following equations. The static magnetic field B_0 leads to a uniform phase for all spins and can be neglected in the analysis of PGSE-based NMR diffusion experiments [12]. Suppose that the gradient pulse pattern is of total duration T; then the so-called echo condition $\int_0^T \boldsymbol{G}(t)\, dt = 0$ has to be fulfilled.

During application of a magnetic field gradient $\boldsymbol{G}(t)$ the precession or Larmor frequency ω is space dependent and is given by $\omega(\boldsymbol{r},t) = \gamma B(\boldsymbol{r},t)$. Thus, the phase Φ is affected by the Brownian motion of the spin-bearing molecules in this spatially and temporally varying magnetic field $B(\boldsymbol{r},t)$. A spin following a path described by the random variable $\boldsymbol{r}(t)$ acquires a phase $\Phi_\delta = \gamma \int_0^\delta \boldsymbol{G}(t)\cdot\boldsymbol{r}(t)\, dt$ during any time δ during which the gradient is applied. Assuming a constant gradient during this time interval this relation can be rewritten as

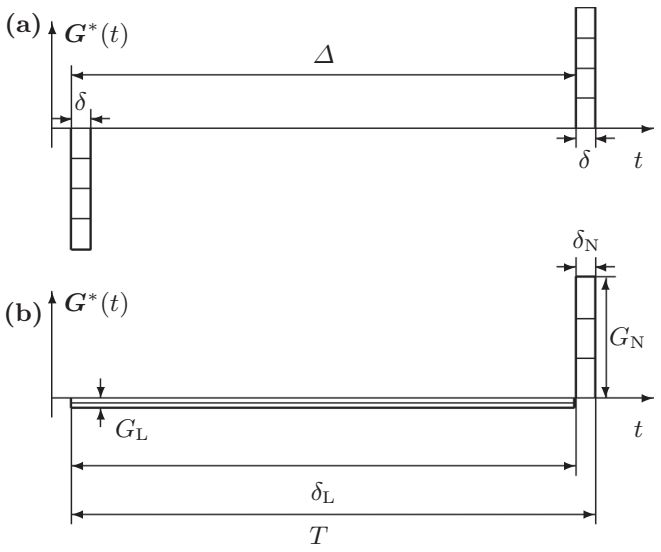

FIG. 1. Effective gradient schemes of diffusive-diffraction PGSE NMR with two stepwise incremented narrow gradients of length δ and with observation time Δ (a). Long-narrow PGSE NMR effective gradient scheme where one of the narrow gradients is extended in length to δ_L with reduced amplitude G_L, which is balanced by a narrow and intense gradient pulse of length δ_N [6]. The time T is defined as the total duration of the gradient pulse scheme (b).

$$\Phi_\delta = 2\pi\boldsymbol{q}\cdot\frac{1}{\delta}\int_0^\delta \boldsymbol{r}(t)\, dt. \tag{3}$$

Diffusive-diffractive PGSE NMR experiments such as published in Ref. [3] consist of two magnetic-field gradient pulses of duration δ with opposite polarity separated by the time Δ and incremented stepwise as shown in Fig. 1(a). Note that Fig. 1 shows the effective gradient pulse scheme $\boldsymbol{G}^*(t)$ as experienced by the spin system [21]. The polarity of the gradients in the laboratory reference frame $\boldsymbol{G}(t)$ will differ from $\boldsymbol{G}^*(t)$ depending on the applied rf pulse scheme (not shown). However, only $\boldsymbol{G}^*(t)$ is needed for the analysis of PGSE NMR diffusion experiments [20]. The observation time Δ is commonly used in PGSE NMR diffusion studies and is related to the total duration of the gradient pulse scheme T by $\Delta = T - \delta$. Equation (3) can be modified to resemble the situation of the diffusive-diffractive PGSE NMR experiment by integrating over the whole time T of the experiment. Since the gradient field is zero in between the two short pulses of length δ the expression can be written as

$$\Phi_{\Delta,\delta} = 2\pi\boldsymbol{q}\cdot\left[\frac{1}{\delta}\int_\Delta^{\Delta+\delta}\boldsymbol{r}_1(t)\, dt - \frac{1}{\delta}\int_0^\delta \boldsymbol{r}_0(t)\, dt\right]. \tag{4}$$

Here $\boldsymbol{r}_1(t)$ and $\boldsymbol{r}_0(t)$ are random variables and describe the position of a spin undergoing Brownian motion in the confining domain. Assuming the narrow gradient pulse approximation is valid [19], i.e., the gradient pulses are short enough to assume $\delta \to 0$ while the area $G\delta$ is kept constant, the time integrals can be replaced by the instantaneous positions at the times of the gradient pulses $\boldsymbol{r}_0(0)$ and $\boldsymbol{r}_1(\Delta)$, leading to

$$\Phi_{\Delta,\delta\to 0} = 2\pi\boldsymbol{q}\cdot[\boldsymbol{r}_1(\Delta) - \boldsymbol{r}_0(0)]. \tag{5}$$

This expression has to be inserted into Eq. (2) and in order to obtain the NMR signal amplitude one has to average over the ensemble of spins. If the gradient separation time is infinitely large $\Delta \to \infty$ the starting and final positions lose their correlation in a closed pore system since the molecules will have traversed the pore space many times. For finite separation time Δ it is enough to require $L^2 \ll D\Delta$ with L being the characteristic dimension of the confining geometry and D the bulk self-diffusion coefficient of the pore filling fluid. Thus, the ensemble average can be calculated for each exponential separately delivering

$$\begin{aligned} E_\infty(\boldsymbol{q}) &= \langle \exp\{-i2\pi \boldsymbol{q}\cdot\boldsymbol{r}_1\}\rangle \langle \exp\{i2\pi \boldsymbol{q}\cdot\boldsymbol{r}_0\}\rangle \\ &= S_0(\boldsymbol{q}) S_0^*(\boldsymbol{q}) \\ &= |S_0(\boldsymbol{q})|^2, \end{aligned} \tag{6}$$

where we used Eq. (1) in the first step. Thus, this experiment yields the power spectrum of the form factor while the phase information is lost. Taking into account that a porous sample consists of many pores, one has to average over all pores and the signal is given by $E_\infty(\boldsymbol{q}) = \overline{|S_0(\boldsymbol{q})|^2}$ [12].

In the PGSE NMR experiment suggested by Laun *et al.* [6] one of the narrow gradient pulses is replaced by a long gradient pulse of duration δ_L with reduced amplitude G_L, see Fig. 1(b). The second gradient pulse is intense with amplitude G_N and narrow with duration δ_N, while the spin-echo condition $G_L\delta_L = G_N\delta_N$ has to be fulfilled for each gradient step. Because of this combination of a long (weak) gradient pulse matched to a conventional narrow gradient pulse Callaghan named this experiment figuratively "long-narrow" [12].

Assuming the short gradient pulse is applied instantaneously $\delta_N \to 0$ such that $\delta_L \to T$, evaluation of Eq. (3) yields

$$\Phi_T = 2\pi \boldsymbol{q}\cdot\left[\frac{1}{T}\int_0^T \boldsymbol{r}(t)dt - \boldsymbol{r}(T)\right], \tag{7}$$

where $\boldsymbol{r}(T)$ is the position of the spin at the time of the narrow gradient. The integral in Eq. (7) can be approximated by replacing any time integral over the position of a random walker with the center of mass of its trajectory [22]. The crucial point of the long-narrow experiment is that in the limit of infinitely long times $T \to \infty$ (or less stringent $DT \gg L^2$) each random walker will have been at every point inside the pore with equal probability. Thus, the center of mass of each trajectory converges to the center of mass position of the pore space $\boldsymbol{r}_{\text{c.m.}}$ [6],

$$\lim_{T\to\infty} \frac{1}{T}\int_0^T \boldsymbol{r}(t)dt = \boldsymbol{r}_{\text{c.m.}}. \tag{8}$$

Equation (7) and Eq. (8) can again be inserted into Eq. (2), leaving the ensemble average to be evaluated. For sufficiently long times T the final position $\boldsymbol{r}(T)$ will be uncorrelated to the prior particle positions and once again one can separate the evaluation of the ensemble average

$$E_\infty(\boldsymbol{q}) = \langle \exp\{i2\pi \boldsymbol{q}\cdot\boldsymbol{r}_{\text{c.m.}}\}\rangle \langle \exp\{-i2\pi \boldsymbol{q}\cdot\boldsymbol{r}(T)\}\rangle. \tag{9}$$

The significant difference to diffusive-diffraction PGSE NMR [comp. Eq. (6)] now becomes apparent. The left term in Eq. (9) yields a complex phase and the right term returns the form factor of the pore space according to Eq. (1). Thus, one arrives at

$$E_\infty(\boldsymbol{q}) = \exp\{i2\pi \boldsymbol{q}\cdot\boldsymbol{r}_{\text{c.m.}}\} S_0(\boldsymbol{q}), \tag{10}$$

which provides the form factor $S_0(\boldsymbol{q})$ multiplied by a complex phase since $E_\infty(\boldsymbol{q})$ is approximately determined by the NMR experiment. The corresponding expression for the pore system can be obtained by averaging over all pores and is given by $E_\infty(\boldsymbol{q}) = \overline{S_0(\boldsymbol{q})}$. Thus, by stepping the gradient amplitudes and recording the spin-echo amplitude (i.e., the echo center) for each gradient step, one acquires the average form factor in the direction of the applied gradients, which upon inverse Fourier transform yields the pore shape function $\rho_0(\boldsymbol{r})$. Thus, this experiment is akin to MRI phase imaging, but with a resolution no longer limited by signal-to-noise. The only remaining limitation, as common for PGSE NMR, is the maximum gradient intensity as generated by the gradient hardware.

B. Resolution

Unlike conventional MRI, signal-to-noise ratio is not the limiting factor for resolution in MRPI, since the signal of the average pore image is arising from the whole sample. However, similar expressions can be derived for the resolution of MRPI q-space imaging as compared to MRI k-space imaging [23]. Analogously to MRI, the nominal resolution of MRPI is given by the highest wave vector $\boldsymbol{q}$ imposed onto the spin system. The pixel size $\Delta x = 1/q_{\max}$ is therefore given by

$$\Delta x = \frac{2\pi}{\gamma G_{\max}\delta_N}, \tag{11}$$

where $G_{\max}$ is the highest gradient amplitude applied and δ_N is the length of the narrow gradient pulse. Note that if the gradients are applied with both polarities, the value for $G_{\max}$ needs to be multiplied by 2 to account for the extra information gained by scanning q-space symmetrically.

Equation (11) is valid for the long-narrow PGSE NMR pulse sequence in the limit of infinitely long δ_L and infinitesimally short δ_N. Deviations from this limit will lead to artifacts, which need to be accounted for in the image analysis [24].

First, the length of long gradient δ_L may not be long enough to ensure that the limit $D\delta_L \gg L^2$ holds. In this case, the phase distribution of the spins in the pore space cannot be approximated as a δ function anymore and one has to re-evaluate the first term in Eq. (9). Instead, the phase distribution function after the long gradient pulse will take on a Gaussian shape. The width of this distribution can be calculated using the Gaussian phase approximation [18] or determined by Monte Carlo simulation [25] and other matrix-based techniques [26,27]. Laun *et al.* [24] give an estimation for the length of δ_L such that the width of this phase spread σ_x is smaller than the pixel size Δx

$$\delta_L \geqslant 1000\Delta x^2/(6D). \tag{12}$$

A violation of this criterion will lead to a blurring of the final image.

Second, if the narrow gradient has a finite width δ_N one may observe an enhancement of the signal near the pore walls [22]. This effect is well known from diffusive-diffractive PGSE NMR [22] and NMR microscopy [28–31] and has been called

edge enhancement. During the time δ_N the molecules may diffuse a distance comparable to or larger than the pixel size of the pore image. Molecules which are located near the wall at the beginning of the gradient pulse are likely to be reflected and directed towards the center of the pore. Thus, there will be a region of depleted signal close to the wall. Moreover, due to conservation of the total signal there will be a region of increased intensity shifted towards the center of the pore. An empirical formula for the distance from the boundary of the signal maximum x_{max} can be derived from the equations found by Mitra *et al.* [22] for the case of parallel planes and is given by [24]

$$x_{max} = 0.5926\sqrt{D\delta_N}. \tag{13}$$

Note that this position will be shifted further towards the center of the pore in case the blurring effect is present. This may be rationalized when considering that the edge enhanced image has to be convoluted with the Gaussian function which describes the phase distribution at the end of the long gradient. Since the edge enhanced image has approximately constant intensity inside the pore and zero outside, the convolution with a Gaussian will shift the area of the increased signal intensity further towards the pore center.

C. Description of MRPI by multiple correlation function (MCF) approach

The multiple correlation function (MCF) approach to solving the Bloch-Torrey equation has proven to be an efficient way to simulate the PGSE NMR signal amplitude for arbitrary gradient pulse patterns [27] and is discussed in detail in Refs. [24,32]. Thus, we restrict ourselves to the elements necessary for this publication.

The Bloch-Torrey equation for the complex magnetization density $m(\boldsymbol{r},t) = m_x(\boldsymbol{r},t) + i\,m_y(\boldsymbol{r},t)$ is given by

$$\frac{\partial m(\boldsymbol{r},t)}{\partial t} - D\Delta m(\boldsymbol{r},t) + i\,\gamma\beta f(t)\widetilde{B}(\boldsymbol{r})m(\boldsymbol{r},t) = 0. \tag{14}$$

The second term of Eq. (14) describes the influence of diffusion on the magnetization density $m(\boldsymbol{r},t)$ with isotropic self-diffusion coefficient D. The second term accounts for the phase difference accumulation due to the magnetic field,

$$B(\boldsymbol{r},t) = \beta\widetilde{B}(\boldsymbol{r})f(t), \tag{15}$$

which is written as a product of its maximum amplitude β, its normalized spatial profile $\widetilde{B}(\boldsymbol{r})$, and its temporal profile $f(t)$. Note that there are only a few spatial profiles $\widetilde{B}(\boldsymbol{r})$ frequently used in PGSE NMR, like linear [33] or second-order magnetic fields [34–37]. In the dimensionless function $f(t)$ the application of a 180° rf pulse is taken into account by inverting the function $f(t)$ for $t < t_{180°}$ and the echo condition is reformulated to $\int_0^T dt f(t) = 0$.

In this work we restrict the simulations to the case of reflecting pore walls. Thus, the magnetization density fulfills the Neumann boundary condition

$$\frac{\partial}{\partial \boldsymbol{n}} m(\boldsymbol{r},t) = 0 \qquad \forall \boldsymbol{r} \in \partial\Omega, \tag{16}$$

where $\partial/\partial\boldsymbol{n}$ denotes the derivative perpendicular to the boundary of the confining domain Ω.

One ansatz for solving Eq. (14) is to expand the magnetization density $m(\boldsymbol{r},t)$ in the basis of eigenfunctions $u_n(\boldsymbol{r})$ of the Laplace operator,

$$m(\boldsymbol{r},t) = \sum_n^\infty c_n(t)u_n(\boldsymbol{r}), \tag{17}$$

with integer index $n = 0,1,2,\ldots$. The eigenfunctions $u_n(\boldsymbol{r})$ are given by

$$\Delta u_n(\boldsymbol{r}) = -\frac{\lambda_n}{L^2}u_n(\boldsymbol{r}) \qquad \forall \boldsymbol{r} \in \Omega, \tag{18}$$

with the dimensionless eigenvalues λ_n and L again the characteristic dimension of the confining domain, e.g., the radius of a cylinder.

To find the coefficients $c_n(t)$ one substitutes Eq. (17) into the Bloch-Torrey equation [Eq. (14)], multiplies with the complex conjugate of the eigenfunctions $u_n^*(\boldsymbol{r})$ and integrates over the domain Ω. The resulting set of ordinary differential equations is given by

$$\frac{d}{dt}c_n(t) + \frac{D\lambda_n}{L^2}c_n(t) + i\,\gamma\beta L\sum_{n'=0}^\infty \mathcal{B}_{n,n'}c_{n'}(t) = 0, \tag{19}$$

where $\mathcal{B}$ is an infinite dimensional matrix given by

$$\mathcal{B}_{n,n'} = \int_\Omega d\boldsymbol{r}\, u_n^*(\boldsymbol{r})\tilde{B}(\boldsymbol{r})u_{n'}(\boldsymbol{r}). \tag{20}$$

The coefficients $c_n(t)$ can be combined into an infinite-dimensional vector $C(t)$ which allows us to rewrite Eq. (19) in matrix representation as

$$T\frac{d}{dt}C(t) + (p\Lambda + i\,q_G\mathcal{B})C(t) = 0. \tag{21}$$

In the last step, two new dimensionless quantities were introduced: the reduced self-diffusion coefficient $p = DT/L^2$ and the generalized gradient intensity $q_G = \gamma\beta TL$. We followed the notation used by Laun *et al.* [24] and denote the generalized gradient intensity as q_G to discern it from the gradient wave vector $\boldsymbol{q}$. Here the diagonal matrix of dimensionless eigenvalues was defined as $\Lambda_{n,n'} = \delta_{n,n'}\lambda_n$. Equation (21) has the solution

$$C(t) = \exp\{-(p\Lambda + i\,q_G\mathcal{B})t/T\}C(0)\,. \tag{22}$$

The NMR signal E can be obtained by integrating Eq. (17) over the domain Ω. Assuming that the detection coil has a homogeneous detection profile, one arrives at

$$\begin{aligned} E &= \int_\Omega m(\boldsymbol{r},t)d\boldsymbol{r} = \sum_{n=0}^\infty c_n(t)\int_\Omega u_n(\boldsymbol{r})\mathrm{d}\boldsymbol{r} \\ &= V\sum_{n=0}^\infty c_n(t)c_n(0). \end{aligned} \tag{23}$$

Substituting the solution already found for the vector $\boldsymbol{C}(t)$ [Eq. (22)] one arrives at

$$\begin{aligned} E &= V\boldsymbol{C}^*(0)\exp\{-(p\Lambda + i\,q_G\mathcal{B})t/T\}\boldsymbol{C}(0) \\ &= \boldsymbol{U}^*\exp\{-(p\Lambda + i\,q_G\mathcal{B})t/T\}\boldsymbol{U}, \end{aligned} \tag{24}$$

where a new vector $\boldsymbol{U} = V^{1/2}\boldsymbol{C}(0)$ has been introduced. At $t = 0$ the magnetization density is uniform, which is equivalent

to assuming that there is no relaxation prior to the onset of the gradient and thus one has

$$m(\boldsymbol{r},t=0)=\frac{1}{V}, \tag{25}$$

where V is the volume of the confining domain Ω. The initial condition given by Eq. (25) implies that

$$c_{\mathrm{n}}(0)=V^{-1/2}\delta_{\mathrm{n},0}. \tag{26}$$

Therefore, $\boldsymbol{C}(0)$ has only one entry in case of the Neumann boundary condition and one can reduce Eq. (24) by taking the first diagonal element given by

$$E=[\exp\{-(p\Lambda+iq_{\mathrm{G}}\mathcal{B})t/T\}]_{0,0}. \tag{27}$$

In case the temporal profile deviates from $f(t)=1$, one can subdivide the interval $[0,T]$ into a number of subintervals K of duration $\tau=T/K$. Then, $f(t)$ is equal to $f(k\tau)$ on the k^{th} sub-interval by approximating the temporal profile as piece wise constant on these subintervals. The signal is then found by evaluating the ordered matrix product

$$E\approx\left[\prod_{k=1}^{K}\exp\{-(p\Lambda+iq_{\mathrm{G}}f(k\tau)\mathcal{B})\tau/T\}\right]_{0,0}. \tag{28}$$

One has to compute the matrices $\mathcal{B}$ and Λ for the chosen domain Ω and spatial profile $B(\boldsymbol{r})$ only once. The time dependence (the usual experimental variation) of the magnetic field then can be approximated by Eq. (28) and its influence on the NMR signal E can be studied.

It is worth noting that the initial magnetization might not be uniform, e.g., due to strong surface relaxation following the excitation rf pulse. This effect has been omitted here, since under weak surface relaxivity conditions as found in our samples the magnetization can be approximated as being homogeneous. The rf coil may also introduce a spatial filter function or pick-up function. However, with our rf coil design the pick-up function is homogeneous in the region of interest. This more general description, including nonuniform magnetization profiles and nonuniform rf and pick-up functions, is discussed in the above-stated references but was not necessary for the evaluation of our case.

D. Phase incremented echo train acquisition (PIETA)

In our communication [10] we introduced the MRPI pulse sequence, which uses a train of 180° rf pulses. This approach may introduce destructive coherence pathways which are dependent on the experimental setup. Baltisberger *et al.* [38] suggested a new phase cycling scheme that allows one to unambiguously extract desired coherence pathways from experiments relying on CPMG like rf pulse schemes. This approach is called phase incremented echo train acquisition (PIETA), because the phase of every other refocusing pulse Φ_{P} is incremented in unison from scan to scan. In conventional CPMG experiments one acquires the signal in the dimensions of echo count n and the time t after the last refocusing pulse, which yields the signal $E(n,t)$. PIETA adds another dimension to CPMG experiments in the direction of the incremented phase Φ_{P} and thus the signal is given by the matrix $E(n,t,\Phi_{\mathrm{P}})$. The signal can be reduced back to two dimensions by applying a Fourier transform of the signal with respect to this phase Φ_{P},

$$E(n,t,\Delta P)=\int E(n,t,\Phi_{\mathrm{P}})e^{-i\Delta P\Phi_{\mathrm{P}}}d\Phi_{\mathrm{P}}, \tag{29}$$

followed by extracting the desired cumulative coherence transfer pathway difference ΔP. ΔP depends on the echo count n according to the desired pathway equation $\Delta P(n)$. The result is the two-dimensional signal $E(n,t)$ containing only intensity from the selected pathway related to the selected cumulative coherence transfer difference $\Delta P(n)$.

We note that the number of scans with PIETA has to be at least 2 times the number of rf pulses in order to unambiguously extract the direct coherence pathway. Thus, this phase scheme comes at an expense of experimental time but naturally provides a much increased signal-to-noise ratio.

III. EXPERIMENTAL

A. MRPI pulse sequence design

1. 1D-MRPI

In order to achieve the limiting condition $D\delta_{\mathrm{L}}\gg L^2$, the length of the long gradient δ_{L} may need to be on the order of several 100 ms or more. During this time δ_{L} the magnetization has to reside in the transverse plane and is therefore subject to experimental limitations as discussed below. Thus, the long-narrow PGSE NMR pulse sequence may have to be adapted to utilize and extend the available time most efficiently.

The limitations as imposed by the instruments and the sample can be categorized as follows:

(a) Internal gradients: Self-diffusion of spin-bearing molecules in an internal gradient leads to an additional coherence loss and thus increases the effective transverse relaxation rate $1/T_2^{\mathrm{eff}}$ [39].

(b) Gradient nonlinearities and offsets: The gradient strength may not scale linearly with the current output of the gradient amplifier. Furthermore, any voltage offset may render bipolar gradients nonsymmetric. Both effects can lead to mismatches and a distorted echo formation as well as additional spin-echo attenuation [40].

(c) Eddy currents: Ring down of the current in the gradient system may lead to gradient mismatches and additional spin-echo attenuation [40].

(d) Concomitant fields: According to Maxwells equations, any magnetic field gradient has to be accompanied by an additional gradient field perpendicular to the applied gradient field. If uncompensated concomitant fields may also lead to echo distortions and additional spin-echo attenuation [41,42].

One may note that in diffusive-diffractive PGSE NMR some of the above-stated effects may have none or only little effect due to the symmetry in the gradient pulse pattern. For example, concomitant fields will be equally strong if two identical, but opposite, gradient pulses are applied and thus their effect is compensated [41,42].

One method to reduce these effects for nonsymmetric gradient pulse patterns as utilized in long-narrow PGSE NMR is to employ a Carr-Purcell-Meiboom-Gill- (CPMG) like pulse sequence [43]. CPMG-like pulse sequences are characterized by a leading 90° rf pulse followed by a train of 180° rf pulses

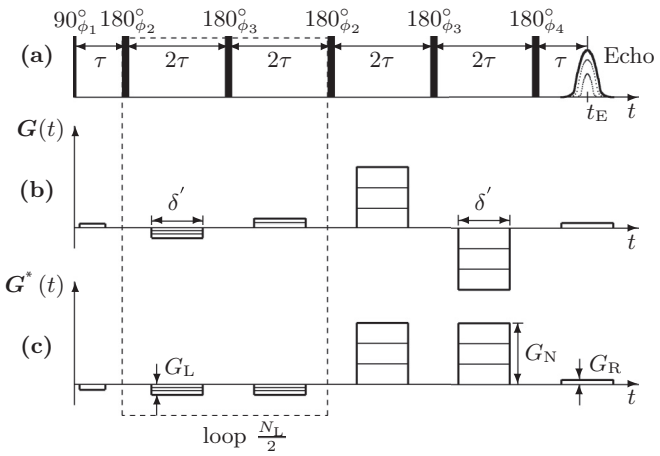

FIG. 2. 1D-MRPI pulse sequence with a CPMG like rf pulse scheme (a). The long gradient is replaced by N_L gradient pieces with gradient amplitude G_L and the narrow gradient was split into two intense gradient pulses with gradient amplitude G_N. The gradients are shown relative to each other as applied in the laboratory reference frame [$\boldsymbol{G}(t)$] (b). The effective gradient pulse scheme $\boldsymbol{G}^*(t)$ shows that the gradient pulses G_L add up and are balanced by the two gradient pulses G_N (c). In practice the gradient pulses are ramped in order to reduce eddy currents (not shown).

each separated by twice the initial 90°–180° rf pulse separation (2τ).

One crucial feature of the CPMG pulse sequence is that in case an internal gradient $\boldsymbol{g}$ is present, its influence is partially refocused halfway between two 180° rf pulses. The effective transverse relaxation rate is given by [43,44]

$$\frac{1}{T_2^{\text{eff}}} = \frac{1}{T_2} + \frac{1}{3} D(\gamma \boldsymbol{g} \tau)^2 . \tag{30}$$

The second term in Eq. (30) describes the influence of the self-diffusion of spin-bearing molecules in the internal gradient $\boldsymbol{g}$ on the effective transverse relaxation rate. Through variation of τ and its extrapolation to zero the effect of self-diffusion on the transverse relaxation rate can be minimized [21,45]. Figure 2(a) shows the CPMG like rf pulse sequence as utilized in this work. The rf pulse phases Φ_i are adapted for the special requirements of the MRPI approach as discussed below. In order to apply the CPMG concept to long-narrow PGSE NMR, the long gradient (G_L) was split into a succession of short gradient pulses of length δ', which were applied centered between the 180° rf pulses [Fig. 2(b)]. Similarly, the narrow gradient pulse G_N was split into two intense gradient pulses each of duration δ'. It is important to note that in the laboratory reference frame the gradients were applied in alternating polarity, such that their effect on the spin system is cumulative. The effective gradient pulse scheme $\boldsymbol{G}^*(t)$ as seen by the spin system is schematically shown in Fig. 2(c). The influence of the internal gradient $\boldsymbol{g}$ is partially refocused as required (not shown). The effective pulsed gradient $\boldsymbol{G}^*(t)$ consists of N_L gradient pieces of strength G_L which are balanced by two narrow gradients with gradient strength G_N. In this work we employed two narrow gradients as well as an even number N_L of long gradient pieces to ensure that gradient nonlinearities and offsets are canceled with each second gradient pulse. Additionally, all gradients were ramped to reduce eddy currents and to ensure a controlled gradient pulse shape (not shown in Fig. 2).

TABLE I. Phase cycle for the CPMG based MRPI pulse sequence. The rf phases Φ_i correspond to the rf pulses according to Fig. 2(a).

Pulse phases				
ϕ_1	ϕ_2	ϕ_3	ϕ_4	Rec. phase
x	x	$-x$	y	$-x$
x	y	$-y$	x	x
x	$-x$	x	$-y$	$-x$
x	$-y$	y	$-x$	x

Furthermore, we introduced read gradients G_R in the interval between the leading 90° and the first 180° rf pulse and during acquisition, see Figs. 2(b) and 2(c). The acquisition of the spin echo in the presence of the read gradient allows one to monitor the echo position in the time domain [46]. This approach is vital to detect gradient mismatches and for separating the wanted signal from unwanted coherence pathways.

The introduction of many rf pulses can give rise to unwanted spin echoes due to additional coherence pathways [47], especially if the rf pulses are applied in inhomogeneous fields as they are common in porous materials. Unwanted coherence pathways can be filtered either using phase cycling [48,49] or using gradient pulses [50]. The MRPI pulse sequence utilizes a distinct gradient pattern which limits the number of contributing coherence pathways if the gradient amplitudes are sufficiently high.

Nonetheless, there are remaining coherence pathways which are unaffected by these gradients. An example is the stimulated echo pathway, which is stored by the first 180° rf pulse in the z direction until it is transformed into detectable signal by the last 180° rf pulse, where both rf pulses partially act as 90° pulses. Such unwanted signals were detected in the time domain. Rf pulses involved in the generation of these coherence pathways were identified by observing the intensity of the spurious spin echos in the time domain while changing the length of selected 180° rf pulses. The phase cycle as shown in Table I was subsequently designed to compensate for these contributions. The number of phase increments was restricted to four steps to keep experiment time within acceptable limits, especially if the pulse sequence is used for multidimensional MRPI experiments as will be discussed in Sec. III A 2 and Sec. III A 3.

We note that especially for low-gradient amplitudes this phase cycle is not sufficient to cancel all unwanted coherence pathways. More elaborate phase schemes such as the PIETA phase-cycling approach may have to be applied in these cases.

2. 2D-MRPI

It is delightful to recognize that the MRPI pulse sequence is in fact an imaging pulse sequence in disguise [24]. As such, it becomes apparent that the narrow gradient G_N acts similarly to the imaging gradient in purely phase-encoded MRI. In MRPI G_N imprints a phase proportional to the distance of the spins to

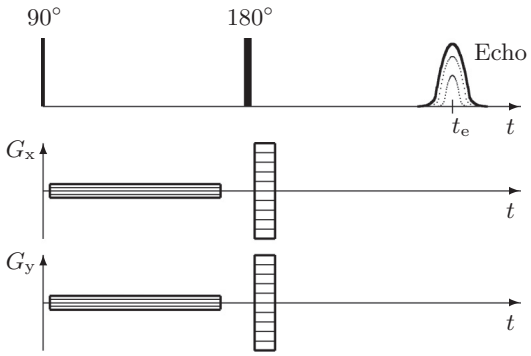

FIG. 3. 2D-MRPI pulse scheme. Gradients G_x and G_y are stepped independently. In practice, the gradient pattern and rf pulse pattern were replaced with the MRPI pulse pattern (using alternating gradients) shown in Fig. 2. It was omitted here for clarity.

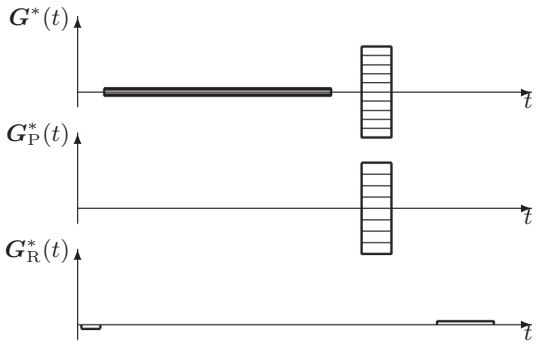

FIG. 4. MRPI-mapping pulse sequence for acquisition of the spatial distribution of pore shapes and sizes mapped onto MRI images. Effective gradients of the MRPI part $G^*(t)$ are stepped for each step of the phase gradient $G^*_P(t)$. The read gradient $G^*_R(t)$ yields the second dimension of the MRI image.

the center of mass of the pores very similar to phase-encoded MRI where the gradient imprints a phase proportional to the distance of the spins, however, in this case to the center of the gradient system.

This similarity can be exploited to sample q-space in whichever experimentally preferred manner. For example, we proposed a two-dimensional MRPI approach [10] in which two gradient pulse patterns are stepped independently to sample q-space point by point on a Cartesian grid. The effective gradient scheme of the two-dimensional version of the MRPI pulse sequence is shown in Fig. 3. This allows us to obtain the average pore image directly by 2D Fourier transformation of the resulting 2D q-space data. In practice, we employed the CPMG-based MRPI pulse sequence with alternating G_x and G_y as discussed in Sec. III A 1.

An alternative approach is to acquire a set of 1D radial q-space profiles which are evenly distributed in a plane not unlike spokes in a wheel. The resulting q-space data have to be Fourier transformed individually to yield a set of real space profiles (projections along the gradient direction) of the sample. Subsequently, a back-projection or Radon transform may be applied to the magnitude data of the real space profiles [51]. This method may provide an advantage in cases where the total experimental time is long since control measurements (such as conventional MRI experiments) can be interspersed between individual profile acquisitions. For example, one may check for long-time drifts of the experimental setup, e.g., by acquiring MRI images of the sample to check for evaporation. Additionally, the simulation using the MCF technique may be faster for 1D profiles in q-space than for the 2D case and a comparison of simulation and experiment may be carried out for individual profiles during acquisition.

3. MRPI mapping

Measuring the spatial distribution of pore sizes is of great relevance in technological applications and for medical diagnosis. One particularly compelling example of the integration of MRPI within the MRI toolbox is the MRPI mapping experiment. It is similar to chemical shift imaging [52]; however, here the MRPI q-space information is mapped onto MRI images instead of the chemical shift.

A conventional MRI pulse sequence typically employs both frequency-encoding and phase-encoding gradients [23]. Figure 4 shows the effective gradient pulse pattern of the MRPI mapping experiment. In the actual experiment the effective gradient $G^*(t)$ is replaced by the CPMG-based MRPI alternating gradient pattern as discussed in Sec. III A 1. In MRPI mapping the read gradient $\boldsymbol{G}_R$ in the beginning and end of the MRPI pulse sequence serves also for the purpose of frequency encoding in read direction. Additionally, a phase gradient $\boldsymbol{G}_P$ is stepped independently to provide the phase encoding of the MRI image. Thus, the experiment proceeds by sampling q-space for each step of the phase gradient $\boldsymbol{G}_P$. A two-dimensional MRI image is acquired and the 1D-MRPI signal is encoded in the third dimension.

B. Challenges imposed by NMR hardware limitations

1. NMR hardware used

NMR measurements were performed on a Bruker Avance 400 spectrometer operating at a proton resonance frequency of 400 MHz. The utilized rf coil had a bird-cage coil design and allowed for a maximum outer diameter of the sample of OD = 1 cm. Typical rf pulse lengths were $t_{90^\circ} = 12.5$ µs and $t_{180^\circ} = 25$ µs when using ^{1}H as the NMR active nuclei in a distilled H_2O sample.

Three Bruker GREAT 60 gradient amplifiers were utilized, each having a maximum current output of 60 A at a digital-to-analog conversion (DAC) resolution of 16 bits. A Bruker Micro 2.5 imaging probe was used to provide gradients in all three Cartesian directions with gradient strengths of 24.2 mT m^{-1}A^{-1}. At the maximum current output of ±60 A the gradient system provided gradient strengths up to $G_{max} = \pm 1.45$ T m^{-1}.

2. Resolution limit of gradient amplifier

Due to the typical length of the long gradient δ_L which may be on the order of several 100 ms, there may be gradient mismatches due to the finite DAC resolution of the gradient amplifier. With a digital resolution of the amplifier limited to 16 bit there are effectively 2^{15} current steps (1 bit is reserved to determine the polarity). Thus the minimal gradient step

is given by $\Delta G^{\min} = 1.45\ \mathrm{Tm}^{-1}/2^{15} = 4.4 \times 10^{-5}\ \mathrm{Tm}^{-1}$. Unfortunately, this minimal step width is far too coarse if one would try to match the long-gradient amplitude to a given amplitude of the narrow gradient. This is easy to rationalize since the calculation of the long-gradient amplitude based on the value of the narrow gradient would require us to match the long gradient with a precision which is increased by the gradient duration ratio δ_L/δ_N. This ratio can easily reach 100 . . . 1000. For this reason, we implemented a program to determine the long-gradient amplitude G_L first using values exactly corresponding to available digital steps. Subsequently, the narrow gradient amplitude G_N was automatically calculated and matched from this information.

3. *Further experimental precautions*

Due to the inductivity of the gradient coils we controlled the rise and fall of the current in the gradient coils by ramping the gradients. In this work we employed a ramp time of 0.1 ms for each gradient pulse. Furthermore, eddy currents may be induced when ramping the gradients, which may lead to changing selectivity of the rf pulses [40]. In order to prevent residual eddy currents during application of the rf pulses a minimum gradient settling time of 0.25 ms after each gradient pulse was implemented in the pulse program.

C. Samples

1. *Calibration samples*

Two different calibration samples were used containing liquids of known self-diffusivity. Sample CAL1 consisted of a cylindrical sample tube of inner diameter ID = 0.8 cm filled with distilled H_2O. Additionally, a second sample (CAL2) was needed to calibrate the pulse sequence at the highest gradient strengths available. For this purpose, a substance with low self-diffusion coefficient was needed. We chose polydimethylsiloxane (PDMS) with a molecular weight of $M_w = 36\,000\ \mathrm{gmol}^{-1}$ in a sample tube of inner diameter of ID = 0.8 cm.

2. *Cylindrical capillaries*

Cylindrical glass capillaries with inner diameters in the micrometer range were utilized in a number of recent studies involving PGSE NMR and NMR methods to extract pore sizes and other parameters [7,10,53–56]. This model porous system is ideally suited to study the influence of the various parameters of the MRPI pulse sequence, since the domain is straightforward to simulate and the inner glass surface leads to a negligible wall relaxation.

The capillaries utilized for sample CYL1 were commercially available cylindrical glass capillaries (Polymicro Inc.) with an inner capillary radius of $L = (10 \pm 1)\,\mu\mathrm{m}$. These particular capillaries consist of a silica core coated with polyimide, yielding an outer diameter of 360 µm. The polyimide coating gives the capillaries some flexibility and allows them to be wound on spools for distribution. Hence, one has to cut the several-meter-long capillary into pieces of the desired length using a sharp knife. For this study a total of 470 capillaries were cut to a length of 5 cm each.

Subsequently, for sample CYL1, the capillaries were loosely stacked and submerged in distilled H_2O for filling by capillary forces. The bath was heated to the boiling point in order to remove residual gas trapped in the capillaries. After removing the stack from the water bath, excess water in the intercapillary spaces was removed by manual drying. The closed pore system was designed by stacking all capillaries in a glass sample tube of inner diameter ID = 0.8 cm [10]. Conventional MRI images were taken of the stacks cross section at different heights of the sample in order to ensure that no NMR signal arises from the intercapillary spaces.

A second sample CYL2 containing two capillary diameters was prepared for the MRPI mapping experiments presented in Sec. IV D. This sample was prepared by creating two compartments filled with capillaries of different diameters by inserting a polymer sheet in the middle of the glass sample tube. Both compartments were filled with capillaries of cylindrical shape; however, their radii for the two compartments differed and were $L_1 = (10 \pm 1)\,\mu\mathrm{m}$ and $L_2 = (5 \pm 1)\,\mu\mathrm{m}$, respectively.

3. *Hemiequilateral triangular capillaries*

Low-symmetry pore shapes of micrometer size pose an additional challenge for the construction of suitable phantoms. For this work, we chose a hemiequilateral triangular shape, since its MCF parameters necessary for MRPI simulations have recently been calculated [24]. The mechanical requirements on the final sample are high since the pore shape dimensions have to be of high precision to prevent additional blurring of the average pore image. Additionally, all capillaries have to be prepared with the same orientation such that the average pore image resembles the underlying pore shape.

The method used was microgroove pattern machining by excimer laser dragging [57]. With this method, the excimer laser is guided perpendicular onto the mask containing the desired pattern as shown in Fig. 5. When the laser impinges on the triangular mask, the laser beam will go through the

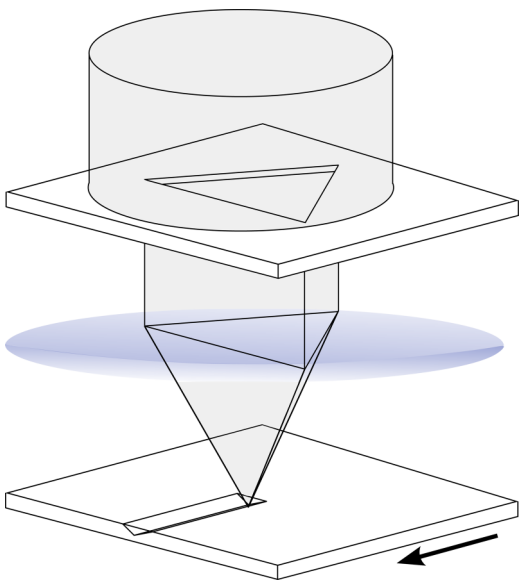

FIG. 5. (Color online) Scheme of microgroove pattern machining by excimer laser dragging. The arrow indicates the direction of movement of the work piece with respect to the laser.

transparent portion of the mask onto the work-piece surface and ablate the work piece. The pattern may be machined into the mask at convenient macroscopic dimensions and then demagnified by a projection lens to the desired dimension of the pattern on the work piece. The desired groove is created by moving the work piece laterally with respect to the laser, while the laser is firing. The arrow in Fig. 5 indicates the direction of movement of the work piece with respect to the laser. The laser ablates material from the work piece with an ablation depth proportional to the exposure time and the fluence F of the laser. Thus, the depth of the groove in the work piece is proportional to the height of the mask pattern in the scanning direction and it is inversely proportional to the movement velocity. Additionally, the width of the grooves in the work piece L will be given by the width of the mask pattern divided by the demagnification factor.

For this work, a triangular mask with sides of lengths 400, 796, and 845 μm was machined into chrome on quartz using a custom JPSA micromachining stage (model IX-100) and an 800-nm, 110-fs pulsed laser (1-kHz Coherent Legend Elite) with a 50-μm-diameter circular spot. The mask was projected at 20× demagnification with an excimer laser (248 nm, 5 ns, $F = 3\,\mathrm{J\,cm^{-2}}$, 500 Hz, Coherent Xantos XS) onto the work piece [175-μm-thick amorphous polycarbonate (APC), Makrofol]. The piece was then translated in a direction perpendicular to the side of length 400 μm at $1.2\,\mu\mathrm{m\,s^{-1}}$ to create 40 rows of 50-mm-long, hemiequilateral triangular grooves with the desired characteristic width of $L = 20$ μm and 80 μm spacing (Fig. 6). Dichloromethane (DCM) has proven to be an effective solvent for chemically welding amorphous polycarbonate [58] but care must be taken to overcome deformations during the chemical welding process. A blank APC sheet was exposed to DCM vapor for 3 min (22 °C, atmospheric pressure) and applied to the machined surfaces to create sets of closed capillaries (Fig. 6). Two of these sets were exposed to DCM vapor on their flat sides to bond them to one another and form the final chips containing 80 channels (2 layers of 40 channels each, with all triangular channels oriented in the same direction). The final product

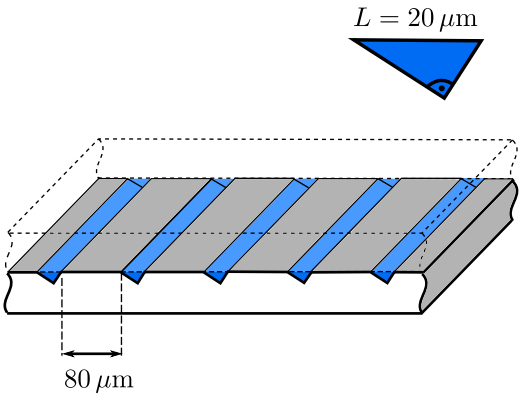

FIG. 6. (Color online) Hemiequilateral triangular pores and their alignment into an ordered array. The characteristic width of a channel, $L = 20$ μm, is indicated for one channel cross section (top). Forty channels separated by 80 μm were machined into APC sheets. Closed hemiequilateral channels were created by bonding a flat polycarbonate sheet on top of the array (dotted line).

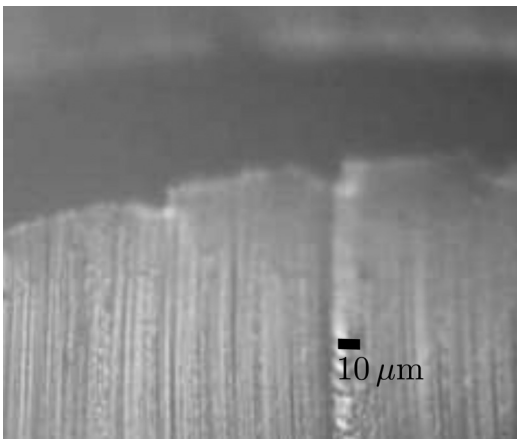

FIG. 7. Optical microscope image of the channel cross section for two exemplary triangular capillaries. The flat polycarbonate sheet delaminated during cutting of the stack and thus there is a black region and the channels appear to be open. The intact samples used for our MRPI experiments contained only closed channels as verified by MRI images of the sample cross section of samples filled with water.

was clamped and allowed to cure slowly over 2 days at room temperature.

Figure 7 shows an optical microscope image of the cross section of two exemplary channels. In order to prepare the array for optical microscopy, the stack had to be cut with a sharp knife, which led to a delamination of the flat sheet and thus the channels appear to be open (dark gray region in Fig. 7). Filling with distilled water was carried out by submersion of the whole chips into a water bath. Subsequently, vacuum was applied over the water phase to remove residual air in the channels by degassing. After sufficient degassing had occurred the vacuum was removed to allow the filling of the capillaries with distilled water. In order to maximize the signal-to-noise ratio for the NMR experiments, a total of four of these filled chips were stacked in a sample tube of diameter $d = 1$ cm. Thus, the final sample (TRI) contained a total of 320 microchannels of the same orientation and size. It should be noted that no effort was made to arrange the pores in the array periodically. In fact, the four chips are only aligned such that the pores have the same orientation across the sample but do not necessarily lead to a periodic arrangement of the pores in a latticelike fashion.

The sample was characterized using standard MRI images to ensure that signal was only coming from inside the pores and that the pores were isolated from each other.

IV. RESULTS AND DISCUSSION

A. Free diffusion

1. Calibration

In order to test whether the given NMR setup is suitable to apply long weak gradients, which are refocused by short intense gradients, we measured the unrestricted self-diffusion of sample CYL1, whose self-diffusion coefficient is known from the literature [59]. To check whether the hardware is working as expected we derived an analytical expression for the expected spin-echo decay. In this context it is convenient to hold all experimental parameters in the wanted expression by

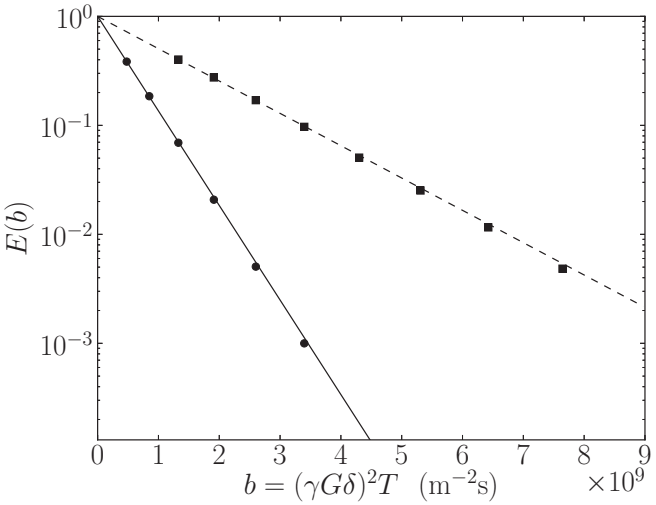

FIG. 8. Comparison of spin-echo attenuation of the unaltered long-narrow PGSE NMR experiment (squares) versus the diffusive-diffractive PGSE NMR experiment (circles) for sample CAL1. The slopes of the fits for the long-narrow PGSE NMR experiment (dashed line) and the diffusive-diffraction PGSE NMR experiment (solid line) yield a ratio of 0.34.

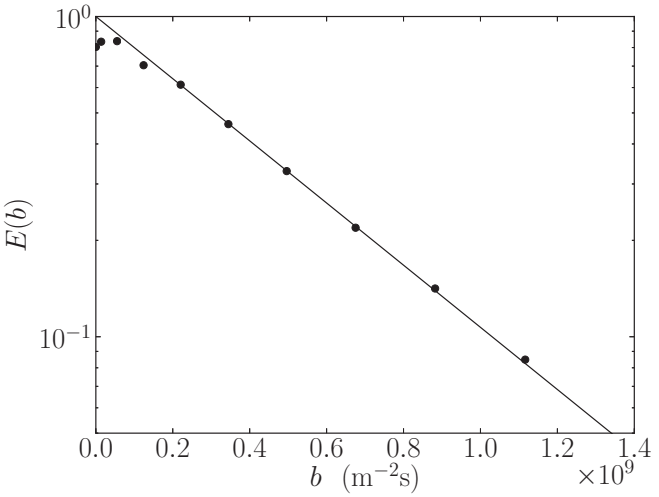

FIG. 9. 1D-MRPI pulse sequence applied to measure free diffusion of H_2O (dots). A fit of the data with Eq. (34) yields a self-diffusion coefficient of $D = 2.2 \times 10^{-9}$ m^2 s^{-1} (solid line).

one single b value [60]. In this case, the spin-echo amplitude for unrestricted Gaussian self-diffusion is given by

$$E = \exp\{-bD\}. \tag{31}$$

The influence of gradients on the spin-echo amplitude E can be calculated with the double time integral over the effective pulsed gradient pattern $\boldsymbol{G}^*(t)$ [20,60]

$$b = \gamma^2 \int_0^t dt' \left[\int_0^{t'} dt'' \boldsymbol{G}^*(t'') \right]^2. \tag{32}$$

The b factor for the unaltered long-narrow PGSE NMR pulse scheme [as shown in Fig. 1(b)] as found by evaluating Eq. (32) in the limit $T \gg \delta$ is given by $b_{\mathrm{LN}} = (\gamma G\delta)^2 T/3$. Thus, it is related to the b factor of the diffusive-diffractive PGSE NMR pulse scheme [as shown in Fig. 1(a)] by

$$b_{\mathrm{LN}} = \frac{b_{\mathrm{PGSE}}}{3}. \tag{33}$$

Hence, the spin-echo attenuation of the long-narrow PGSE NMR experiment for a given gradient amplitude G is reduced by a factor of 3 as compared to diffusive-diffractive PGSE NMR. Figure 8 shows a comparison for the spin-echo attenuation of the unaltered long-narrow PGSE NMR pulse sequence as shown in Fig. 1(b) (squares) and the diffusive-diffractive PGSE NMR pulse sequence as shown in Fig. 1(a) (circles) with the sample CAL1 at a temperature of $T_{\mathrm{K}} = 293$ K. In both cases a spin-echo rf pulse scheme [61] was utilized consisting of a leading 90° and a refocusing 180° rf pulse. The gradient parameters were $\delta = 2$ ms, $\Delta = 50$ ms for the PGSE NMR experiment and $\delta_{\mathrm{L}} = 50$ ms, $\delta_{\mathrm{N}} = 2$ ms for the long-narrow PGSE NMR experiment. Respective data in Fig. 8 were fitted against b_{LN} and b_{PGSE}, yielding consistent self-diffusivities of $D_{\mathrm{LN}} = 2.04 \times 10^{-9}$ m^2 s^{-1} (dashed line) and $D_{\mathrm{PGSE}} = 2.00 \times 10^{-9}$ m^2 s^{-1} (solid line), verifying the validity of the derived b factors. Furthermore, the ratio of the two slopes in Fig. 8 equates to 0.34 which is close to 1/3 predicted by Eq. (33).

2. 1D-MRPI calibration

In the case of the MRPI pulse sequence as shown in Fig. 2(b), evaluation of Eq. (32) leads to a more complex expression for the b value in the case of unrestricted Gaussian diffusion. The corresponding b factor for the 1D-MRPI pulse sequence based on CPMG applying $\int_0^T G^*(t)dt = 0$ is given by

$$b = \frac{(\gamma G_{\mathrm{N}} 2\delta')^2}{3} \left[\delta'(N_{\mathrm{L}} + 2) + \delta_{\mathrm{s}} \left(\frac{2N_{\mathrm{L}}^2 + 3N_{\mathrm{L}} + 1}{2N_{\mathrm{L}}} + \frac{3}{4} \right) \right], \tag{34}$$

where δ_{s} is the separation between the gradient pulses, i.e., the time from the end of one gradient pulse until the leading edge of the next gradient pulse. Equation (34) reduces to Eq. (33) in the limit of $\delta_{\mathrm{s}} \to 0$ and $\delta'(N_{\mathrm{L}} + 2) = T$. The effect of the gradient pulse ramps is partially accounted for by adding one ramp time to the gradient pulse duration δ'.

Figure 9 shows the application of the 1D-MRPI pulse sequence attempting to measure unrestricted self-diffusion in sample CAL1 at a temperature of $T_{\mathrm{K}} = 293$ K. The parameters of the MRPI pulse sequence were $N_{\mathrm{L}} = 40$, $\delta' = 2$ ms, $2\tau = 2.5$ ms, $\delta_{\mathrm{s}} = 0.5$ ms, and $G_{\mathrm{N}}^{\max} = 0.175$ Tm^{-1}. A fit of the experimental data yields a self-diffusion coefficient of $D = (2.2 \pm 0.2) \times 10^{-9}$ m^2 s^{-1}, consistent with a literature value of $D = 2.0 \times 10^{-9}$ m^2 s^{-1} [59] within uncertainties.

While the omission of the first couple of data points in Fig. 9 and a smaller signal-to-noise ratio as compared to the data presented in Fig. 8 do not allow for a smaller uncertainty, the difference might also be explained by not taking into account the extra term in the b factor arising from the gradient ramp times, a correction term well known in PGSE NMR diffusion experiments [62]. In this study we chose to ignore this term,

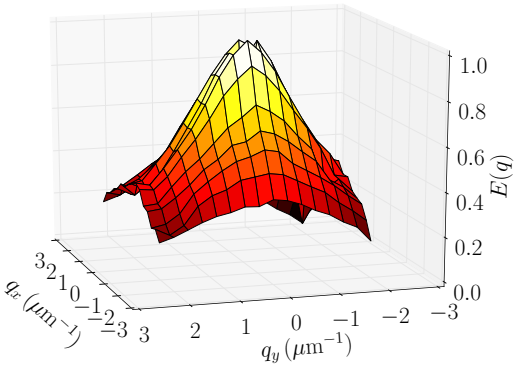

FIG. 10. (Color online) 2D-MRPI applied to PDMS. Shown is the spin-echo maximum in the time domain obtained by sampling q-space on a Cartesian grid.

since we were foremost concerned with obtaining a Gaussian attenuation in case of free diffusion as well as a stable spin echo in the time domain with each pulsed gradient step. The spin-echo attenuation shows a depression of the spin-echo amplitude of the first four data points. This phenomenon is more pronounced when more 180° rf pulses are utilized. This can be explained by destructive coherence pathways that are created by imperfect rf pulses, which are dephased by the gradient pulses once they are applied at sufficiently high gradient strengths. These points have been excluded from the fit. We will return to this signal depression in more detail in Sec. IV B 1.

3. 2D-MRPI calibration

MRPI may require the maximum gradient strength available with the current gradient system. In this case, the high self-diffusion coefficient of H_2O of sample CAL1 would lead to a too strong attenuation of the spin-echo signal. Thus, a substance with small diffusivity was necessary to achieve sufficient signal-to-noise even for highest gradient strengths G_N. The sample CAL2 contains highly viscous PDMS and is therefore ideally suited. Figure 10 shows a surface plot of the magnitude of the spin-echo maxima obtained when applying the 2D-MRPI pulse sequence to the sample CAL2. The parameters used were $N_L = 36, \delta' = 4.6$ ms, $\delta_s = 0.9$ ms, $G_N^{max} = 1.45$ Tm^{-1}, and $T_K = 293$ K. The observed spin-echo attenuation exhibits rotational symmetry around the axis $(q_x,q_y) = (0,0)$, as expected for isotropic Gaussian self-diffusion. A fit along the one-dimensional contour at $q_x = 0$ yields a self-diffusion coefficient of $D = 1.0 \times 10^{-12}$ m^2 s^{-1} which lies in the expected range according to Ref. [63] and is consistent with a diffusion measurement utilizing a PGSE NMR stimulated echo pulse sequence. Note that a 1D-MRPI experiment was performed as well to observe the spin-echo signal in the time domain up to the highest gradient strengths (not shown in Fig. 10). Furthermore, we secured that the spin-echo position and spin-echo shape in the time domain is stable for all gradient amplitudes (data not shown).

B. 1D-MRPI

1. Cylindrical capillaries

Gradients in the one-dimensional MRPI pulse sequence were applied perpendicularly to the symmetry axis of the

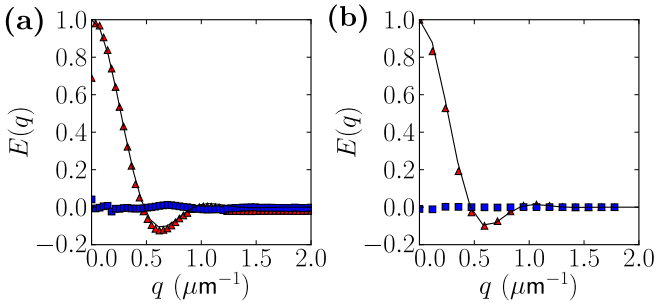

FIG. 11. (Color online) Real (triangles) and imaginary part (squares) of the q-space profile of sample CYL1 as obtained by the 1D-MRPI pulse sequence. The spin-echo amplitude is distorted at low gradient strengths due to destructive coherence pathways (a). The PIETA rf pulse phase scheme allows us to extract the direct pathway and to recover the points at low gradient strengths (b). The solid lines was obtained by MCF simulation for both figures.

cylinders of the sample CYL1. The q-space data are shown in Fig. 11(a). The phase between the real and imaginary parts of the signal is either 0° or 180° in agreement with the symmetry of the confining domain. The number of long gradient pulses was $N_L = 36$ with gradient durations of $\delta' = 3.045$ ms (including one ramp time) and the separation between the 180° rf pulses was $2\tau = 5.56$ ms.

As discussed in Sec. III A, at low gradient strengths additional coherence pathways may contribute to the signal. In order to recover the correct signal intensity we applied the PIETA rf pulse phase scheme [38]. For this purpose the rf pulse phases Φ_2 and Φ_4 were incremented from 0 to 2π in 64 steps. The other rf pulse phases were kept constant at $\Phi_1 = \Phi_{rec} = 0$ and $\Phi_3 = \pi/2$, respectively. The resulting data set had dimensions of $512 \times 16 \times 64$, where 512 points were acquired in the time domain, $\boldsymbol{q}$ was incremented in 16 steps, and 64 phase steps were acquired. A subsequent Fourier transform in the phase direction allowed us to extract the direct coherence pathway.

Figure 11(b) shows the complex form factor as obtained by selecting the spin-echo center of the direct coherence pathway for each step in q-space. As predicted, the points for low gradient strength were recovered. Moreover, when comparing the signal amplitude for low $\boldsymbol{q}$ values between Fig. 11(a) and 11(b) one may notice that the imaginary part (squares) is closer to zero in Fig. 11(b) as required by the cylindrical pore shape. Note that the experiment time increases by a factor of 16 when comparing with the four-step phase cycle. Therefore, this phase scheme is not feasible for multidimensional MRPI applications. However, by analyzing the coherence pathway spectrum contributing to the echos, one is, in principle, able to identify the most important spurious coherence pathways. Based on this information one can design shorter but still efficient phase cycles which eliminate these most important pathways, depending on the particular conditions of the experiment.

Figure 12 shows the convergence of the signal $E(q)$ to the form factor $S_0(q)$ with increasing ratio DT/L^2. The total time of the gradient pattern T of the MRPI experiment was increased by increasing the number of long gradient pulses N_L while keeping all other parameters fixed. The MRPI parameters were $2\tau = 4.725$ ms, $\delta' = 4$ ms, and

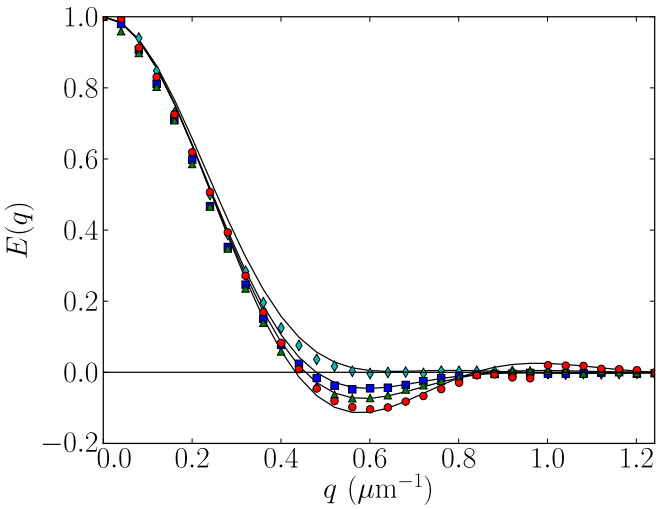

FIG. 12. (Color online) Real part of the normalized spin-echo amplitude $E(q)$ versus wave vector q for increasing ratio DT/L^2. The shown experimental data corresponds to $DT/L^2 = 1.1$ (diamonds), $DT/L^2 = 2.1$ (squares), $DT/L^2 = 3.0$ (triangles), and $DT/L^2 = 5.8$ (circles). MCF simulation for each experiment is shown as a black line.

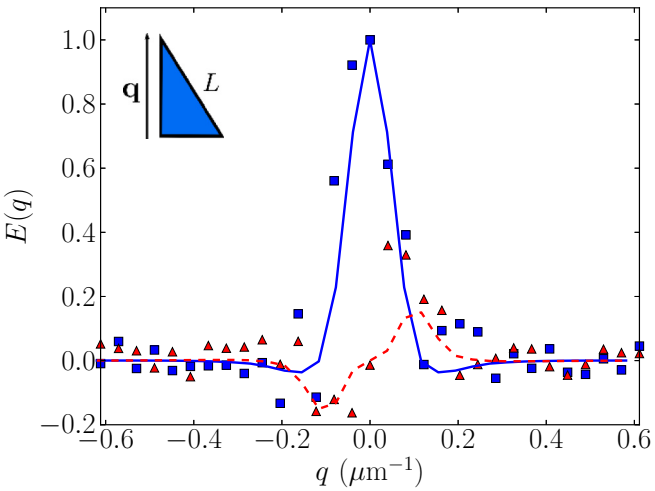

FIG. 13. (Color online) Comparison of experiment and simulation of the q-space profile as obtained when applying a one-dimensional MRPI experiment to the stack of hemiequilateral triangular capillaries.

$G_{\max} = 0.58\ \mathrm{T\,m^{-1}}$. In contrast to the experiments shown in Ref. [10] the sample was not heated but was kept at a temperature of $T_K = 293$ K, leading to a self-diffusion coefficient of $D = 2.0 \times 10^{-9}\ \mathrm{m^2\,s^{-1}}$. The number of long gradient pulses was varied with $N_L = \{10,20,30,50\}$, leading to ratios of $DT/L^2 = \{1.1,2.1,3.0,5.8\}$. Corresponding MCF simulations were carried out and match the experimental results (solid lines in Fig. 12). The spin-echo amplitudes $E(q)$ in Fig. 12 contain the first negative lobe of the form factor even for moderate lengths T of the MRPI gradient pattern. At room temperature the parameters $N_L = 20$ and thus $T = 103$ ms were sufficient to extract useful information about the pore structure. Observation of the second lobe, and therefore more detailed information about the structure, requires more gradient pulses, e.g., $N_L = 50$ and thus $DT/L^2 = 5.8$. Experimental parameter in this work typically satisfy $DT/L^2 \approx 5.8$ by using higher than room temperatures while only employing $N_L = 36$ long gradient pulses.

2. *Triangular capillaries*

MRPI experiments on the hemiequilateral triangular capillary sample TRI pose additional challenges. The amorphous polycarbonate is partially permeable for H_2O molecules. Thus, there is exchange of molecules between the capillary space and the solid matrix during the MRPI experiment. Moreover, there is noticeable surface relaxation at the APC-H_2O interface. Both phenomena have similar effects on the MRPI signal and can be regarded as a finite absorption probability of the diffusing H_2O molecules at capillary boundaries. The experimental determination of the rate constants of both processes is possible but very time consuming and might warrant a study of its own.

To understand the conditions of our setup (including the sample) and to optimize experimental parameters we simulated a series of 1D profiles with the MCF technique using a hemiequilateral triangular domain without surface relaxation. Fixed input conditions were the transverse relaxation time of $T_2 = 600$ ms and the self-diffusion coefficient of $D = 2.0 \times 10^{-9}\ \mathrm{m^2\,s^{-1}}$ for H_2O at a temperature of $T_K = 293$ K. Variable parameters were the number of long gradient pulses, their length, and 2τ. This procedure returned optimized parameters as $2\tau = 6$ ms, $N_L = 26$, and $\delta' = 5.5$ ms corresponding to $T = 168$ ms and an effective narrow gradient length of $2\tau + \delta' = 11.5$ ms.

Subsequently, a one-dimensional MRPI experiment was performed, acquiring the real part (squares) and imaginary part (triangles) of the q-space as shown in Fig. 13. Data were obtained from the center of the spin echos in the time domain for each gradient step. The orientation of the capillary with respect to the $\boldsymbol{q}$ vector is indicated in the insert of Fig. 13. The solid and dashed lines show the real and imaginary parts as obtained by MCF simulation. Parameters of the MCF simulation were identical to the experimental parameters; however, the gradient pulses were approximated to be rectangular, while their length included one ramp time. Simulation and experiment agree qualitatively. Differences can be explained by residual irregularities in the capillary geometry due to the manufacturing process and the inherent noise in experimental data. However, experiment and simulation show the correct phase behavior, which includes values that differ from 0° and 180°. Thus, Fig. 13 shows the measurement of the complex one-dimensional form factor of a triangular domain on the micrometer scale.

C. 2D-MRPI

1. *Cylindrical capillaries*

The 2D-MRPI pulse sequence was applied to the sample CYL1 with the capillary radius $L = (10 \pm 1)\,\mu$m. The gradients q_x and q_y were stepped independently in 32 steps each up to a maximum gradient strength of $G_{\max} = \pm 1.45\ \mathrm{T\,m^{-1}}$ as already reported in Ref. [10].

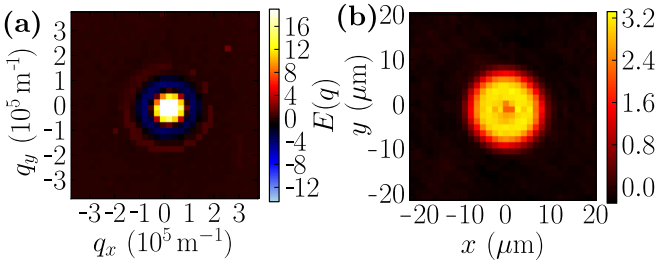

FIG. 14. (Color online) Real part of the two-dimensional form factor as acquired with MRPI from water in a bundle of capillaries (a) and the corresponding averaged pore image obtained by a subsequent 2D-Fourier transform of this data matrix (b). Replot from Ref. [10].

Figure 14(a) shows a surface plot of the real part of the two-dimensional q-space data. The data contain both positive and negative values and resemble the two-dimensional form factor of the underlying pores of cylindrical shape. The average pore image [Fig. 14(b)] was obtained by a 2D Fourier transform of the q-space data and plotting the phased real part of the resulting image. Further experimental parameters can be obtained from Ref. [10].

The circular cross section of the cylindrical capillaries has been imaged at a nominal resolution of 1.3 μm. Figure 15 (dots) shows the cross section through the pore image at $y = 0$. The solid line in Fig. 15 shows the same cross section as obtained by MCF simulation with a cylinder radius of $L = 10$ μm which is consistent with the experimental data. In particular, the effects of edge enhancement and blurring are convincingly reproduced by the MCF approach. Such agreement cannot be achieved by considering the edge enhancement according to Eq. (13) alone (assuming a locally flat surface). With an effective duration of the narrow gradient of $2\tau + \delta' = 8.6$ ms, Eq. (13) would predict a peak $x_{\max} = 3.1$ μm away from the surface. However, comparison with Fig. 15 shows that the peaks are shifted even further towards the center of the pore due to the finite length of the long gradient as discussed in Sec. II B.

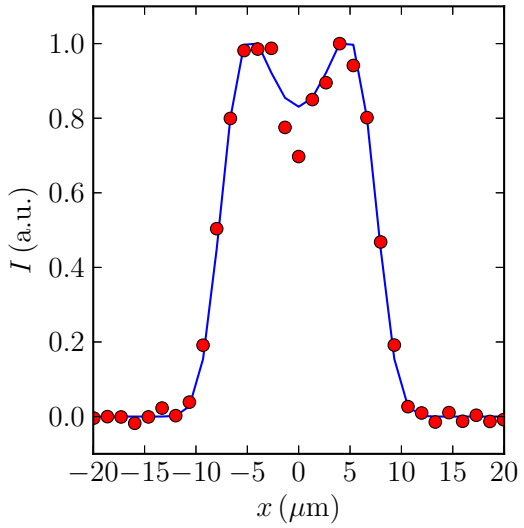

FIG. 15. (Color online) One-dimensional cross section through the 2D-MRPI image at $y = 0$ (dots) and MCF simulation (solid line).

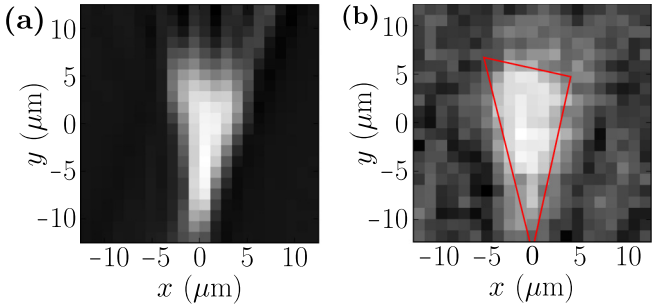

FIG. 16. (Color online) Image simulated with MCF technique (a) and experimental image obtained by Radon transform of the one-dimensional Fourier transformed q-space profiles (b).

MCF simulations are based on the same set of parameters as used for the experiments. In particular, the full MRPI gradient scheme was incorporated in the MCF simulation. Thus, the effects of edge enhancement and blurring were captured. The only free parameter in the simulation was the radius of the pores. Thus, one may incorporate the MCF simulation into a least-squares fit algorithm and fit the dimensions of an unknown sample.

2. *Triangular capillaries*

Due to the unknown absorption rate of the spins at the H_2O-APC interface, we simulated the expected MRPI image for the hemiequilateral triangular domain using the MCF approach with a set of reasonable experimental parameters without wall relaxation. Figure 16(a) shows the expected image for triangular capillaries where surface relaxation has been neglected. The image shows the shape of the underlying pore structure. Due to the limited time of the long gradient the image appears blurred.

We chose to acquire 2D-MRPI images using the back-projection–Radon transform approach. The permeability of the polycarbonate sheet allows for H_2O molecules to leave the pore space. Therefore, we verified between the individual MRPI profiles that the capillaries were still filled with water. For this purpose we acquired conventional MRI images of the sample cross section at different heights of the sample. The one-dimensional MRPI pulse sequence was applied in 18 directions. The resulting q-space data were Fourier transformed and subsequently subjected to a back-projection which yielded the two-dimensional image.

Figure 16(b) shows the first MRPI image of a non-point-symmetric pore shape at the micrometer scale. As a guide to the eye, the expected triangular shape is indicated. While the signal-to-noise ratio is limited the hemiequilateral triangular shape has been recovered. When comparing Fig. 16(b) with the optical microscope image in Fig. 7 one may note the rounded edges in the actual sample, which are captured by the MRPI image. Additionally, the finite surface relaxation leads to further blurring of the image.

Remarkably, the presence of finite surface permeability and surface relaxation did not pose an insurmountable barrier to the application of MRPI. In fact, the presence of these effects in the sample TRI may be regarded as a starting point for a systematic study of the effect of surface relaxivity and surface

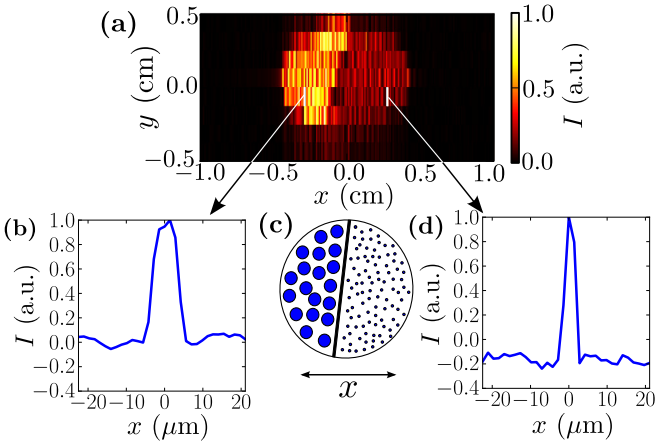

FIG. 17. (Color online) Mapping of average pore images on the MRI image. Shown are the two imaging dimensions x and y. The MRPI encoding was applied in the third dimension (not shown). The Fourier transform of the MRPI q-space profile is shown for two exemplary pixels (arrows). The profile width yields the right pore diameters of $L_1 = 20\,\mu$m (b) and $L_2 = 10\,\mu$m (d). The sketch shows the cross section through the whole sample (a) and the sketch of the two compartments filled with two sizes of cylindrical capillaries (c).

permeability and the required MRPI parameters. This may aid in the method development for the eventual application to natural porous media in material and life science.

D. MRPI mapping

The MRPI mapping pulse sequence was applied to the capillary sample CYL2 containing two sizes of capillaries. Figure 17(a) shows the two-dimensional MRI image of the cross section of sample CYL2. This image was obtained by 2D-Fourier transformation of the MRI encoded image for the first step in the MRPI gradient sequence ($\boldsymbol{q} = 0$). The two-dimensional matrix consisted of 512 points in the the time domain under influence of the read gradient G_R and eight steps in the domain of the phase gradient G_P. The width of the circular profile in the MRI image agrees with the actual inner diameter of the sample tube of ID = 8 mm. Figure 17(c) shows a sketch of the transverse cross section through the sample. Note that the sketch is not to scale and many more capillaries were contained in the sample tube. In the sketch, the direction x indicates in which direction the read gradient $\boldsymbol{G}_\mathrm{R}$ was applied. The two compartments of different capillary diameters can be distinguished by an increased signal intensity for the side with the larger capillaries. It is worth noting that the higher signal intensity is solely caused by the larger volume of H_2O present in the large capillaries rather than a higher number of capillaries per pixel.

The MRPI signal was Fourier transformed for two exemplary pixels, see Figs. 17(b) and 17(d). The arrows indicate the location of the MRI pixels from which the pore images were extracted. The dimensions of the large [Fig. 17(b)] and small capillaries [Fig. 17(d)] were recovered when taking into account edge enhancement and blurring.

It is intriguing to see that the signal-to-noise ratio of the profiles is on the order of 10 although only a few capillaries are present in each MRI voxel. This is a consequence of the increased signal-to-noise ratio of MRPI as compared to diffusive-diffractive PGSE NMR, since $S_0(\boldsymbol{q})$ is measured instead of $|S_0(\boldsymbol{q})|^2$. This may render MRPI more robust and versatile for combinations with MRI in mapping experiments.

Thus, one is able to map the average pore shapes as well as sizes present within a given voxel onto MRI images, which allows us to combine the resolution of MRPI with the spatial information of MRI. In principle, one may perform four-dimensional (2D × 2D) experiments where for each pixel of the MRI image a full two-dimensional MRPI image is acquired. In the 4D MRPI mapping approach one would apply the full 2D-MRPI pulse sequence for each imaging phase gradient step. The 2D-Fourier transform of the MRI k-space data at zero MRPI gradient ($\boldsymbol{q} = 0$) would yield the MRI image. Another 2D-Fourier transform of the q-space data would yield the average pore image for each voxel in the MRI image. However, the cylindrical symmetry of the underlying pore structure in the present study would not yield any additional information about the sample and a 3D approach is sufficient.

V. CONCLUSIONS

The MRPI approach is a recent tool to acquire average pore images and to determine the sizes and shapes of a porous system with closed pores. While stimulated echo pulse sequences appear to be attractive for samples with $T_1 \geqslant T_2^{\mathrm{eff}}$ one needs to rationalize that the accumulation of spatially distributed phase differences only occur in the presence of magnetic field gradients while the magnetization resides in the x,y plane. Only in this case will the average phase converge to the center-of-mass phase [comp. Eq. (8)]. Hence, when the magnetization is stored in the z direction the phase accumulation does not progress. Therefore, stimulated echo techniques are not favorable for MRPI, although they might be applicable with recently suggested double-wave-vector techniques [9]. However, MRPI may be chosen due to better performance in low signal-to-noise situations and thus advanced pulse sequences such as discussed in this contribution may be needed to utilize and extend the available time most efficiently. If the condition of convergence $D\delta_\mathrm{L} \gg L^2$ is met one is rewarded with the higher information content of the average form factor and the ensuing ability to acquire true images of the average pores [6,10,11].

Here we demonstrate together with a parallel study focusing on triangular domains [11] that MRPI can be applied to arbitrary pore shapes and down to sizes on the micrometer scale. MRPI can inherit a wealth of proven concepts from the MRI toolbox when exploiting its similarity to MRI phase-encoded imaging. In particular, the acquisition of q-space data can be carried out point by point and thus advanced trajectories already developed for MRI k-space imaging such as compressed sensing [64] could be adopted for MRPI.

Moreover, the signal-to-noise ratio with MRPI is improved by up to an order of magnitude as compared to diffusive-diffraction PGSE NMR, since $S_0(\boldsymbol{q})$ is measured instead of $|S_0(\boldsymbol{q})|^2$. This provides more opportunities when combining a multitude of NMR or MRI approaches with MRPI. For example, we demonstrated that measuring the MRPI signal inside an individual voxel of an MRI image is feasible. The

application of MRPI mapping can obtain valuable information on heterogeneous materials with spatial distributions of pore sizes and shapes. While methods for the mapping of local pore sizes have been introduced [65,66], MRPI mapping provides the local averaged pore shape as the more fundamental characterization of the porous system.

ACKNOWLEDGMENTS

We gratefully acknowledge financial support by the Ministry of Business, Innovation and Employment of New Zealand. S.H. thanks Victoria University of Wellington for receiving support through a Ph.D. scholarship. We furthermore thank Dr. Andrew Coy for helpful discussions.

[1] P. Mansfield and P. Morris, *NMR Imaging in Biomedicine*, Vol. 12, Supplement 2 of Advances in Magnetic Resonance (Academic Press, New York, 1982).
[2] P. T. Callaghan, *Principles of Nuclear Magnetic Resonance Microscopy* (Clarendon Press, Oxford, 1991).
[3] P. T. Callaghan, A. Coy, D. Macgowan, K. J. Packer, and F. O. Zelaya, Diffraction-like effects in NMR diffusion studies of fluids in porous solids, Nature **351**, 467 (1991).
[4] J. Als-Nielsen and D. McMorrow, *Elements of Modern X-ray Physics* (Wiley, Chichester, 2011).
[5] D. Svergun, L. Feĭgin, and G. Taylor, *Structure Analysis by Small-Angle X-Ray and Neutron Scattering* (Plenum Press, New York, 1987).
[6] F. B. Laun, T. A. Kuder, W. Semmler, and B. Stieltjes, Determination of the defining boundary in nuclear magnetic resonance diffusion experiments, Phys. Rev. Lett. **107**, 048102 (2011).
[7] N. Shemesh, C.-F. Westin, and Y. Cohen, Magnetic resonance imaging by synergistic diffusion-diffraction patterns, Phys. Rev. Lett. **108**, 058103 (2012).
[8] V. G. Kiselev and D. S. Novikov, Comment on "magnetic resonance imaging by synergistic diffusion-diffraction patterns," Phys. Rev. Lett. **110**, 109801 (2013).
[9] T. A. Kuder and F. B. Laun, NMR-based diffusion pore imaging by double wave vector measurements, Magn. Reson. Med. **70**, 836 (2013).
[10] S. Hertel, M. Hunter, and P. Galvosas, Magnetic resonance pore imaging, a tool for porous media research, Phys. Rev. E **87**, 030802 (2013).
[11] T. A. Kuder, P. Bachert, J. Windschuh, and F. B. Laun, Diffusion pore imaging by hyperpolarized xenon-129 nuclear magnetic resonance, Phys. Rev. Lett. **111**, 028101 (2013).
[12] P. T. Callaghan, *Translational Dynamics & Magnetic Resonance* (Oxford University Press, Oxford, 2011).
[13] G. A. Barrall, L. Frydman, and G. C. Chingas, NMR diffraction and spatial statistics of stationary systems, Science **255**, 714 (1992).
[14] P. P. Mitra, P. N. Sen, L. M. Schwartz, and P. Le Doussal, Diffusion propagator as a probe of the structure of porous-media, Phys. Rev. Lett. **68**, 3555 (1992).
[15] J. Snaar and H. VanAs, NMR self-diffusion measurements in a bounded system with loss of magnetization at the walls, J. Magn. Reson. A **102**, 318 (1993).
[16] P. Callaghan, Pulsed-gradient spin-echo NMR for planar, cylindrical, and spherical pores under conditions of wall relaxation, J. Magn. Reson. A **113**, 53 (1995).
[17] D. C. Douglass and D. W. McCall, Diffusion in paraffin hydrocarbons, J. Phys. Chem. **62**, 1102 (1958).
[18] C. H. Neuman, Spin echo of spins diffusing in a bounded medium, J. Chem. Phys. **60**, 4508 (1974).
[19] E. O. Stejskal, Use of spin echoes in a pulsed magnetic-field gradient to study anisotropic, restricted diffusion and flow, J. Chem. Phys. **43**, 3597 (1965).
[20] F. Stallmach and P. Galvosas, in *Annual Reports on NMR Spectroscopy*, Vol. 61 (Elsevier, Amsterdam, 2007), pp. 51–131.
[21] R. F. Karlicek and I. J. Lowe, A modified pulsed gradient technique for measuring diffusion in the presence of large background gradients, J. Magn. Reson. **37**, 75 (1980).
[22] P. P. Mitra and B. I. Halperin, Effects of finite gradient-pulse widths in pulsed-field-gradient diffusion measurements, J. Magn. Reson. A **113**, 94 (1995).
[23] M. A. Bernstein, K. F. King, and X. J. Zhou, *Handbook of MRI Pulse Sequences* (Elsevier Academic, London, 2004).
[24] F. B. Laun, T. A. Kuder, A. Wetscherek, B. Stieltjes, and W. Semmler, NMR-based diffusion pore imaging, Phys. Rev. E **86**, 021906 (2012).
[25] E. Toumelin, C. Torres-Verdin, B. Sun, and K.-J. Dunn, Random-walk technique for simulating NMR measurements and 2d NMR maps of porous media with relaxing and permeable boundaries, J. Magn. Reson. **188**, 83 (2007).
[26] P. T. Callaghan, A simple matrix formalism for spin echo analysis of restricted diffusion under generalized gradient waveforms, J. Magn. Reson. **129**, 74 (1997).
[27] D. S. Grebenkov, NMR survey of reflected Brownian motion, Rev. Mod. Phys. **79**, 1077 (2007).
[28] B. Pütz, D. Barsky, and K. Schulten, Edge enhancement by diffusion: microscopic magnetic resonance imaging of an ultrathin glass capillary, Chem. Phys. Lett. **183**, 391 (1991).
[29] B. Pütz, D. Barsky, and K. Schulten, Edge enhancement by diffusion in microscopic magnetic resonance imaging, J. Magn. Reson. **97**, 27 (1992).
[30] P. Callaghan, A. Coy, L. Forde, and C. Rofe, Diffusive relaxation and edge enhancement in NMR microscopy, J. Magn. Reson. A **101**, 347 (1993).
[31] T. De Swiet, Diffusive edge enhancement in imaging, J. Magn. Reson. B **109**, 12 (1995).
[32] D. S. Grebenkov, Laplacian eigenfunctions in NMR. I. A numerical tool, Concepts Magn. Reson. A **32**, 277 (2008).
[33] W. S. Price, Pulsed-field gradient nuclear magnetic resonance as a tool for studying translational diffusion: Part I. Basic theory, Concepts Magn. Reson. **9**, 299 (1997).
[34] P. Le Doussal and P. N. Sen, Decay of nuclear magnetization by diffusion in a parabolic field: An exactly solvable model, Phys. Rev. B **46**, 3465 (1992).
[35] N. M. Loening, J. Keeler, and G. A. Morris, One-dimensional DOSY, J. Magn. Reson. **153**, 103 (2001).
[36] J. P. Stockmann, P. A. Ciris, G. Galiana, L. Tam, and R. T. Constable, O-space imaging: Highly efficient parallel imaging using second-order nonlinear fields as encoding gradients with no phase encoding, Magn. Reson. Med. **64**, 447 (2010).

[37] W. Kittler, P. Galvosas, and M. Hunter, Parallel acquisition of *q*-space using second order magnetic fields for single-shot diffusion measurements, J. Magn. Reson. **244**, 46 (2014).
[38] J. H. Baltisberger, B. J. Walder, E. G. Keeler, D. C. Kaseman, K. J. Sanders, and P. J. Grandinetti, Phase incremented echo train acquisition in NMR spectroscopy, J. Chem. Phys. **136**, 211104 (2012).
[39] B. Robertson, Spin-echo decay of spins diffusing in a bounded region, Phys. Rev. **151**, 273 (1966).
[40] W. S. Price, Pulsed-field gradient nuclear magnetic resonance as a tool for studying translational diffusion: Part II. Experimental aspects, Concepts Magn. Reson. **10**, 197 (1998).
[41] D. G. Norris and J. M. Hutchison, Concomitant magnetic field gradients and their effects on imaging at low magnetic field strengths, Magn. Reson. Imag. **8**, 33 (1990).
[42] M. A. Bernstein, X. J. Zhou, J. A. Polzin, K. F. King, A. Ganin, N. J. Pelc, and G. H. Glover, Concomitant gradient terms in phase contrast MR: Analysis and correction, Magn. Reson. Med. **39**, 300 (1998).
[43] S. Meiboom and D. Gill, Modified spin-echo method for measuring nuclear relaxation times, Rev. Sci. Instrum. **29**, 688 (1958).
[44] H. Y. Carr and E. M. Purcell, Effects of diffusion on free precession in nuclear magnetic resonance experiments, Phys. Rev. **94**, 630 (1954).
[45] J. Kärger, H. Pfeifer, and W. Heink, Principles and application of self-diffusion measurements by nuclear magnetic resonance, Adv. Magn. Reson. **12**, 1 (1988).
[46] P. T. Callaghan, PGSE-MASSEY, a sequence for overcoming phase instability in very-high-gradient spin-echo NMR, J. Magn. Reson. **88**, 493 (1990).
[47] M. D. Hürlimann, Diffusion and relaxation effects in general stray field NMR experiments, J. Magn. Reson. **148**, 367 (2001).
[48] A. D. Bain, Coherence levels and coherence pathways in NMR: A simple way to design phase cycling procedures, J. Magn. Reson. **56**, 418 (1984).
[49] G. Bodenhausen, H. Kogler, and R. Ernst, Selection of coherence-transfer pathways in NMR pulse experiments, J. Magn. Reson. **58**, 370 (1984).
[50] A. Bax, P. De Jong, A. Mehlkopf, and J. Smidt, Separation of the different orders of NMR multiple-quantum transitions by the use of pulsed field gradients, Chem. Phys. Lett. **69**, 567 (1980).
[51] A. Kak and M. Slaney, *Principles of Computerized Tomographic Imaging* (IEEE Press, New York, 1988).
[52] P. Mansfield, Spatial mapping of the chemical shift in NMR, Magn. Reson. Med. **1**, 370 (1984).
[53] A. Bar-Shir, L. Avram, E. Özarslan, P. J. Basser, and Y. Cohen, The effect of the diffusion time and pulse gradient duration ratio on the diffraction pattern and the structural information estimated from *q*-space diffusion MR: Experiments and simulations, J. Magn. Reson. **194**, 230 (2008).
[54] N. Shemesh, E. Özarslan, A. Bar-Shir, P. J. Basser, and Y. Cohen, Observation of restricted diffusion in the presence of a free diffusion compartment: Single- and double-PFG experiments, J. Magn. Reson. **200**, 214 (2009).
[55] D. Benjamini and U. Nevo, Estimation of pore size distribution using concentric double pulsed-field gradient NMR, J. Magn. Reson. **230**, 198 (2013).
[56] G. A. Álvarez, N. Shemesh, and L. Frydman, Coherent dynamical recoupling of diffusion-driven decoherence in magnetic resonance, Phys. Rev. Lett. **111**, 080404 (2013).
[57] H. Hocheng and K.-Y. Wang, Microgroove pattern machined by excimer laser dragging, IJMTM **13**, 241 (2008).
[58] D. Ogonczyk, J. Wegrzyn, P. Jankowski, B. Dabrowski, and P. Garstecki, Bonding of microfluidic devices fabricated in polycarbonate, Lab Chip **10**, 1324 (2010).
[59] M. Holz, S. R. Heil, and A. Sacco, Temperature dependent self-diffusion coefficients of water and six selected molecular liquids for calibration in accurate ^{1}H NMR PFG-measurements, Phys. Chem. Chem. Phys. **2**, 4740 (2000).
[60] E. O. Stejskal and J. E. Tanner, Spin diffusion measurements: Spin echoes in the presence of a time-dependent field gradient, J. Chem. Phys. **42**, 288 (1965).
[61] E. L. Hahn, Spin echos, Phys. Rev. **80**, 580 (1950).
[62] W. S. Price and P. W. Kuchel, Effect of nonrectangular field gradient pulses in the Stejskal and Tanner (diffusion) pulse sequence, J. Magn. Reson. **94**, 133 (1991).
[63] M. Appel and G. Fleischer, Investigation of the chain-length dependence of self-diffusion of poly(dimethylsiloxane) and poly(ethylene oxide) in the melt with pulsed-field gradient NMR, Macromolecules **26**, 5520 (1993).
[64] M. Lustig, D. Donoho, and J. M. Pauly, Sparse MRI: The application of compressed sensing for rapid MR imaging, Magn. Reson. Med. **58**, 1182 (2007).
[65] M. E. Komlosh, E. Özarslan, M. J. Lizak, F. Horkay, V. Schram, N. Shemesh, Y. Cohen, and P. J. Basser, Pore diameter mapping using double pulsed-field gradient MRI and its validation using a novel glass capillary array phantom, J. Magn. Reson. **208**, 128 (2011).
[66] N. Shemesh, G. A. Álvarez, and L. Frydman, Measuring small compartment dimensions by probing diffusion dynamics via non-uniform oscillating-gradient spin-echo (NOGSE) NMR, J. Magn. Reson. **237**, 49 (2013).